THE JOURNAL OF PHYSICAL CHEMISTRY C

Article

pubs.acs.org/JPCC

Prediction of the Dependence of the Fuel Cell Oxygen Reduction Reactions on Operating Voltage from DFT Calculations

Yao Sha, Ted H. Yu, Boris V. Merinov, and William A. Goddard, III*

Materials and Process Simulation Center (139-74), California Institute of Technology, Pasadena, California 91125, United States

ABSTRACT: To use density functional theory (DFT) to seek improved catalysts for the oxygen reduction reaction (ORR) in a proton exchange membrane fuel cell, we developed a systematic way to handle the barriers of electron transfer reactions (e.g., $H^+ + e- + O_{ad} \rightarrow OH_{ad}$) within the DFT framework. We report applications of this new method to determining the dependence for the barriers of various ORR reaction steps on the operating electrochemical potential for the Pt-catalyzed fuel cell. This method is used to estimate the optimum operating potential. In the Article, we show how to estimate the change in efficiency from changes in the reaction barriers. On the basis of our mechanism and calculated barriers, the optimum operating voltage for the ORR on Pt is found to be 0.68 V/NHE, which is close to the standard operating voltage of ~0.8 V/NHE, validating this analysis.

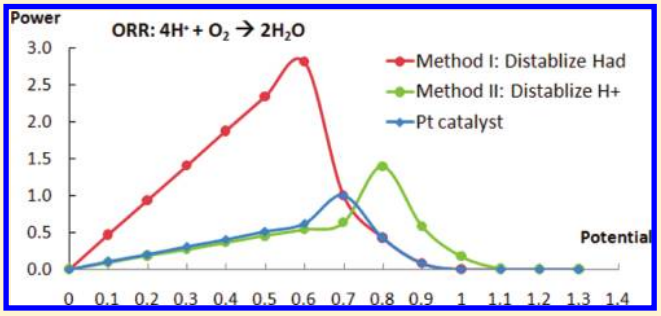

INTRODUCTION

Proton exchange membrane fuel cells (PEMFCs) are efficient, environmentally clean, energy conversion systems suitable for transportation and stationary applications.[1−4] They produce electricity from chemical energy, using fuels (e.g., hydrogen) and oxidants (usually oxygen or air) for electrochemical conversion into water. It is well known that the efficiency of PEMFCs is limited primarily on the cathode side by slow kinetics of the catalytic oxygen reduction reaction (ORR), $^1/_2O_2 + 2H^+ + 2e^- \rightarrow H_2O$. Pt remains the best PEMFC catalyst, but it is expensive and does not provide a sufficient rate for the ORR. To improve this weak link of the fuel cell technology, it is necessary to better understand the mechanism of the ORR under real operating conditions that includes influence of electrode potential. We and others have used the density functional theory (DFT) approach to quantum mechanics (QM) to determine the mechanism for ORR and to determine how the barrier would change for new alloys.[5−11] However, the critical issue of accounting for the dependence of the electron transfer steps on the external electrochemical potential is not yet satisfactory.[6,12−14]

We develop here a systematic approach for handling the electron-transfer step along with the solvation effects and including the effect of the external electrochemical potential on the electron-transfer reactions involved in ORR.

COMPUTATIONAL METHODS

Quantum Mechanics. In this study, we used the SeqQuest code,[15] developed by Schultz, which solves the Kohn-Shan equation self-consistently for periodic systems, while using contracted Gaussian basis sets and angular-momentum-projected norm-conserving nonlocal effective core potentials.[16−19] All calculations used the kinetic and exchange-correlation functional developed by Perdew, Burke, and Ernzerhof (PBE).[20] The Pt (111) surface was represented by a semi-infinite slab with a (2 × 2) unit cell and three layers of atoms. The bottom layer is fixed to approximate the bulk, whereas the top two layers are relaxed to approximate the surface. The real space grid density was 5 points per angstrom, whereas the reciprocal space grid was 5 × 5 × 0 for slab calculations. For the charged systems, the local moment countercharge (LMCC) method[21,22] was used to balance charges and avoid the net charge, dipole, and quadruple.

Solvation. To estimate the solvation effects for the ORR steps, we adopted an implicit continuum solvation method[11] based on the Poisson−Boltzmann equation.[23,24] Our calculations use the coarse grid Adaptive Poisson−Boltzmann Solver (APBS)[25−27] incorporated into the Computational Materials Design Facility (CMDF).[28] The continuum solvation model is widely and successfully applied in cluster calculations.[29−31] In this approach, solvation is modeled as pure electrostatic interactions of the surface and aqueous phase. Intermediates and reaction paths are optimized by DFT, and the resulting Mulliken charge populations serve as input for the implicit solvation calculations. The solvation energy is then directly added as a correction to the enthalpy obtained from gas-phase DFT calculations. These calculations assume that a dielectric constant is 80 and a solvent radius of 1.4 Å. We validated this approach by comparing the calculated implicit solvation energy for systems with known explicit solvation energies for O_{ad}, OH_{ad}, and H_2O_{ad} on Pt.[11] Including solvation effects leads to substantial changes in the favored mechanism for the ORR on Pt.[32] Details of our solvation approach have been reported in ref 11.

Received: August 5, 2011
Revised: February 1, 2012
Published: February 2, 2012

   dx.doi.org/10.1021/jp207526u | J. Phys. Chem. C 2012, 116, 6166−6173

The reaction pathways were optimized using the nudged elastic band (NEB) method.[33,34] Every image along the path was reoptimized for each total charge q (a periodic system may have a partial charge and in our calculations q runs from 0.0e to +1.0e with an increment of 0.1e), and the most stable one was selected as optimal configuration. Similar to Norskov et al.[13] and Neurock et al.,[9,35,36] we also assume that the partial electron, given away by the surface, goes to the Fermi level. This leads to an energy gain of $q\phi_F$, where ϕ_F is the Fermi potential. Therefore, the total energy is calculated as follows

$$E = E_{gas(+q)} + E_{solv} + q\phi_F \quad (1)$$

Comparing each of these images, we identify the transition state (TS) and hence the barrier. Here the energy of every single image depends on the ϕ_F. By varying ϕ_F (modified by the applied electrode potential U), defined as the difference from the Normal Hydrogen Electrode (NHE), we derive the ϕ_F and U-dependent barrier.

Coupling to External Potential. In carrying out these studies, we need to determine the relationship between the electrode potential and work function of the catalyst. To do this, Neurock et al.[9,35] proposed using vacuum as a reference. However, instead we seek to find the absolute value for the Pt electrode at various potentials and use that energy as the Fermi energy (E_F), similar to the Norskov approach.[13] This E_F must be compatible with all other calculations. Because

$$E_{F(U)} = E_{F(NHE)} + eU \quad (2)$$

we simply need to estimate $E_{F(NHE)}$. For this purpose, we use the following reaction cycle

$$H^+(aq) \rightarrow H^+(gas) \rightarrow H^+(gas) + e^- \rightarrow \frac{1}{2}H_2 \quad (3)$$

- The first step is the desolvation of the proton that was calculated to be +11.92 eV,[37] using similar methods.
- The second step involves taking an electron from the Fermi level of the electrode, so the energy cost is exactly $E_{F(NHE)}$.
- The third step requires −15.86 eV, based on our DFT calculation.

Therefore, the total energy cost for $H^+(aq) \rightarrow {}^1/_2H_2$ is

$$11.92\ eV + E_{F(NHE)} - 15.86\ eV = E_{F(NHE)} - 3.94\ eV \quad (4)$$

For U = 0.0 V relative to NHE, we have by definition that enthalpy $H({}^1/_2H_2) = H(H^+_{solv})$. Therefore, $E_{F(NHE)} - 3.94$ eV = 0 eV. Hence, with our method $E_{F(NHE)}$ = 3.94 eV. Compared with the experimentally observed 4.85 eV,[38] this implies a 0.91 eV systematic correction to bring the H^+ and ${}^1/_2H_2$ in balance and make our DFT calculations consistent with experiment.

Summarizing the above discussion, the energy expression becomes

$$E = E_{gas(+q)} + E_{solv} + E_{F(NHE)} + qU \quad (5)$$

where q is the charge in the system and U is an electrode potential relative to NHE.

RESULTS AND DISCUSSION

We consider that the ORR on the Pt(111) surface consists of the following elementary steps (reactions)

$$H^+(aq) + e \leftrightarrow H_{ad} \quad (A)$$

$$O_{2gas} \rightarrow O_{2ad} \rightarrow 2O_{ad} \quad (B)$$

$$O_{ad} + (H^+ + e)/H_{ad} \rightarrow OH_{ad} \quad (C)$$

$$OH_{ad} + (H^+ + e)/H_{ad} \rightarrow H_2O_{ad} \quad (D)$$

As we have discussed elsewhere, for various metals under various conditions, other steps may be more important,[32] but this serves to illustrate the methodology we propose herein.

In addition to solvation effects, reactions A, C, and D should also be corrected for the external chemical potential. It turns out that the barrier for reaction A is mostly enthalpy-dependent.

Hydrogen Reduction Reaction (Volmer Reaction) $H^+ + e \rightarrow H_{ad}$ (Step A of the ORR). The fundamental assumption in the Norskov approach and most other approaches is to calculate the reversible potential for the hydrogen reduction reaction (Volmer reaction[39]) using the following cycle

$$H^+(aq) + e^- \rightarrow \frac{1}{2}H_2 \rightarrow H_{ad} \quad (6)$$

The first step is simply the balance between H^+ and H_2. The reversible potential is defined to be 0.0 V relative to the NHE with identical anode and cathode. Hence, $E(H^+) = E({}^1/_2H_2)$. At an external potential of $+U$, the free energy of H^+ relative to H_2 becomes $-U$. The reaction enthalpy for the second step of reaction 6 is simply the energy difference between ${}^1/_2H_2$ and H_{ad}. Using DFT, we calculate the reaction enthalpy for ${}^1/_2H_2 \rightarrow H_{ad}$ on Pt(111) to be −0.66 eV. Therefore, the total reaction enthalpy for $H^+(aq) \rightarrow H_{ad}$ is $\Delta H[H^+(aq) \rightarrow H_{ad}]_{QM} = -0.66$ eV. The experimental value of $\Delta H[H^+(aq) \rightarrow H_{ad}]_{exp}$ = 0.40 eV[40,41] (based on 1 M H^+). The difference may arise from the dissimilarity between the assumed reference concentration of H_{ad} and that of the surface H_3O^+ and inaccuracies in the DFT calculations of the H_{ad} bond energy. Therefore, DFT gives $D_{e,H/Pt(111)}$ = 2.80 eV, $D_{e,H2}$ = 4.63 eV, and D_O = 4.48 eV (all in gas phase) compared with experimental values of $D_{O,H/Pt(111)}$ = 2.54 to 2.67 eV and $D_{O,H2}$ = 4.48 eV,[42,43] respectively.

For ORR, before H^+ reacts with the surface, H_3O^+ approaches the surface and moves into the first water bilayer. This leads to the ORR step

$$H_3O^+(surface) \rightarrow H_{ad} \quad (7)$$

Using eq 5, we calculate the overall reaction enthalpy ΔH = −0.44 eV. This implies that H_{ad} is preferred at U < 0.44 V. As U increases, the reaction changes from exothermic to endothermic at U = 0.44 V, making H_{ad} less available and leading to an additional barrier for reactions involving H_{ad} at U > 0.44 V. Despite the endothermicity at U > 0.44 V, the Volmer reaction can still proceed as the source of H_{ad}. For sufficiently high electrode potentials, the Volmer step might be the rate-determining step (RDS) for all ORR mechanisms involving H_{ad}.

For the barrier, the reaction path is simply the direct transfer of a proton from H_3O^+ to the surface. Following the procedure described in the Computational Methods section, we carried out DFT calculations of the full reaction path for fixed total charges ranging from 0.0e to +1.0e with an increment of 0.1e (Figure 1) to determine the reaction barriers as a function of

dx.doi.org/10.1021/jp207526u | J. Phys. Chem. C 2012, 116, 6166−6173

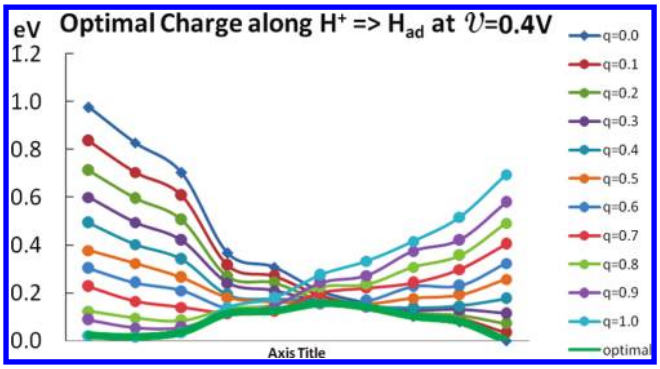

Figure 1. Potential energy surface $H^+ \rightarrow H_{ad}$ with different charges at U = 0.4 V. The left-most point along every curve represents H_3O^+, whereas the right-most point represents H_{ad}. The lowest among all (green bold line) represents optimal charge as the reaction $H^+ \rightarrow H_{ad}$ proceeds at U = 0.4 V.

charge. The corresponding 2-D potential energy surface (PES) is shown in Figure 2 for U = 0.4 V. The optimal reaction path is

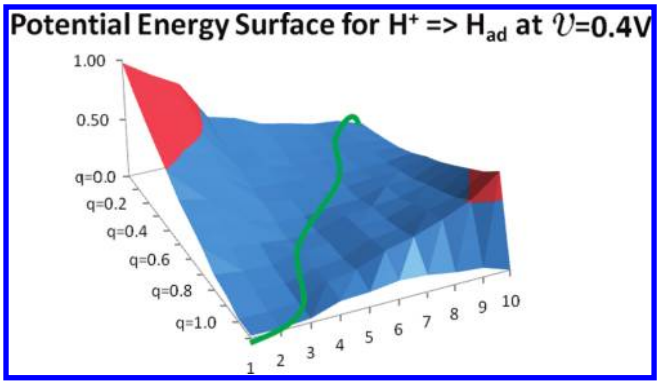

Figure 2. Potential energy surface for the $H^+ \rightarrow H_{ad}$ reaction at U = 0.4 V. The bottom point represents H_3O^+ with charge +1, whereas the point on the top represents H_{ad} with charge 0.0.

shown in Figure 3. It starts from a surface H_3O^+ (q = +1.0) and ends with a H_{ad} (q = 0.0). This gives a barrier of 0.16 eV for q = +0.4.

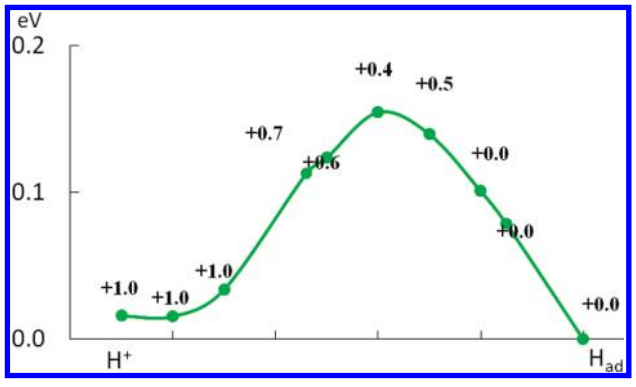

Figure 3. Optimal reaction path for $H^+ \rightarrow H_{ad}$ at U = 0.4 V with charge taken into consideration. We can see that as the reaction proceeds, optimal charge changes from 1.0 to 0.0, representing an electron transferred from the electrode to the H^+.

The energy for each image varies as the electrode potential changes according to eq 5, hence the PES in Figure 3 also varies. Figure 4 shows the PES at 0.0, 0.4, 0.8, and 1.23 V, and

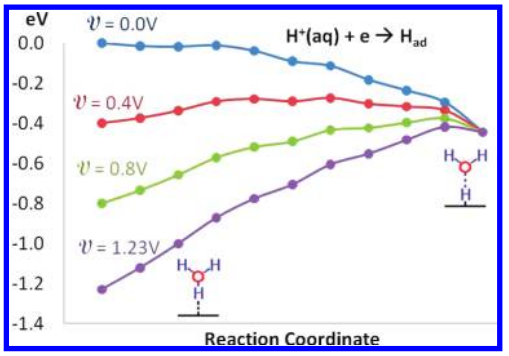

Figure 4. Potential-dependent energy surfaces for $H_3O^+ \rightarrow H_{ad}$.

Figure 5 shows the reaction enthalpy and barrier at various electrode potentials. We see that the reaction is exothermic and

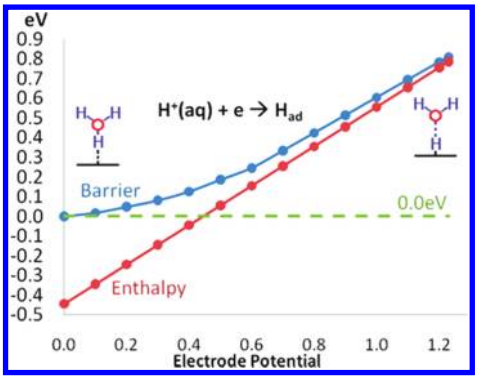

Figure 5. Potential-dependent barriers for $H^+ \rightarrow H_{ad}$.

barrierless at U = 0.0 V. As U increases above 0.1 V, the reaction becomes endothermic and carries a barrier. Under the fuel cell condition, U = 0.8 V, this leads to a barrier of 0.42 eV with ΔH = 0.36 eV.

O_2 Dissociation Reaction $O_2 \rightarrow 2O_{ad}$ (Step B of the ORR). The O_2 dissociation step is a simple surface reaction that does not involve electron transfer, and hence we do not consider this step in detail. In our previous studies,[11,32] we calculated the O_2 dissociation to be barrierless under solvation conditions.

OH Formation Reaction $H_3O^+ + O_{ad} \rightarrow H_2O + OH_{ad}$ (Step C of the ORR). According to Norskov et al.,[13] the reaction enthalpy for reaction C can be calculated as a function of external potential from the following cycle

$$H^+(aq) + O_{ad}(solv) \rightarrow \frac{1}{2}H_2(gas) + O_{ad}(solv) \rightarrow OH_{ad}(solv) \quad (8)$$

The reaction enthalpy for the first step of reaction 8 is defined to be eU. Our DFT calculations show that the second step has ΔH = −0.47 eV, leading to E = −0.47 eV + eU for the whole reaction (Figure 10). With increasing external potential, the reaction becomes endothermic and at U = 0.8 V, ΔH = + 0.33 eV.

This energy includes only the thermodynamic balance between the solution phase H^+ and the O_{ad}, OH_{ad} on the surface. However, the kinetics of the reaction involving H_3O^+ and an electron from the surface to form OH_{ad} is of greater importance. The process starts with H_3O^+ at a site near the surface which reacts with a surface O_{ad}. During this reaction,

dx.doi.org/10.1021/jp207526u | J. Phys. Chem. C 2012, 116, 6166–6173

O_{ad} accepts the proton from H_3O^+ and donates an electron to form OH_{ad}. This leads to

$$H^+(surface) + O_{ad}(solv) + e \rightarrow OH_{ad}(solv) \quad (9)$$

We calculate the reaction enthalpy for this reaction to be $\Delta H = -0.28$ eV + eU. However, since reaction A is exothermic for $U < 0.44$ V, an alternative reaction path should be considered

$$H^+(surface) + O_{ad}(solv) + e \rightarrow H_{ad}(surface) + O_{ad}(solv) \rightarrow OH_{ad}(solv) \quad (10)$$

The first step is just reaction A. The second step does not involve electron transfer; therefore, it is not potential-dependent. Our DFT calculation give $\Delta H = 0.40$ eV for this step.

The preferred pathway is therefore determined by the barrier for both reactions. For reaction 9, we calculated the NEB reaction path for this process with a surface charge $q = 0.0e$ to $+1.0e$ with an increment of $0.1e$. The charge is assumed to go to the Fermi level as described in the Computational Methods section. The correction for the solvation effect is included for all images. On the basis of eq 5, this leads to the PES shown in Figures 6 and 7. The optimal charge is $+1.0e$ for the H^+

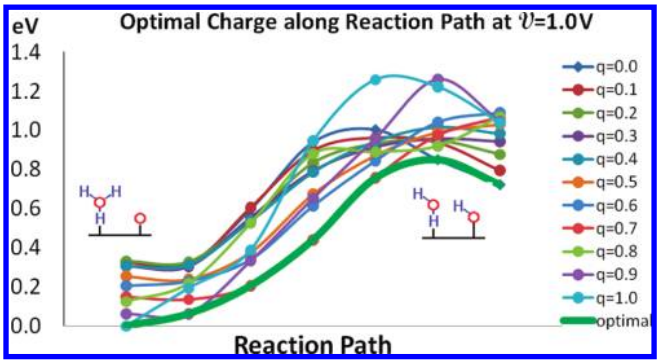

Figure 6. Summary of the reaction path energies of $O_{ad} + H^+ + e^- \rightarrow OH_{ad}$ for various fixed charges at $U = 1.0$ V. The green bold line shows the optimal path.

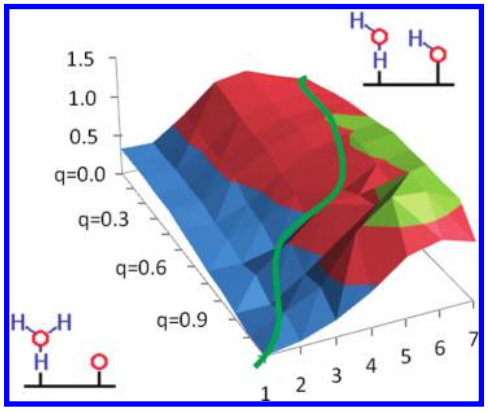

Figure 7. Contour plot of the energy surface for the reaction $O_{ad} + H^+ + e^- \rightarrow OH_{ad}$ in which charge and OH formation are considered as two independent coordinates. The green curve gives an optimal reaction path at $U = 1.0$ V.

reactant and $0.0e$ for the OH_{ad} produced by the reaction. Considering the reaction for various charges, we find the optimal reaction path involving electron transfer, illustrated by the bright green line in both Figures 6 and 7. This leads to Figure 8, the PES for the reaction at $U = 1.0$ V. We can see that the TS is very close to the product. Electron transfer occurs before the reaction reaches the TS. Because the energy for almost every image varies with the electrode potential according to reaction 5, so all curves in Figures 6–8 shift as

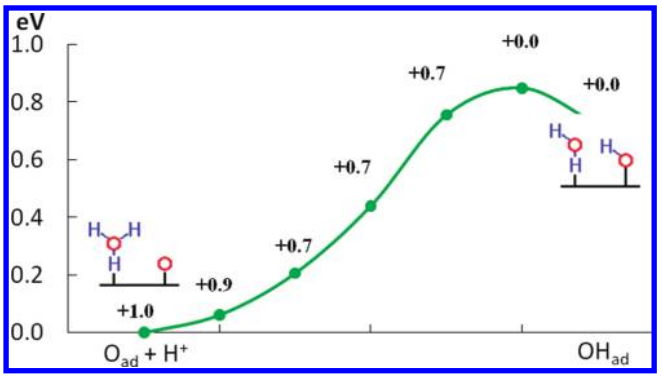

Figure 8. Optimal reaction energy surface for $O_{ad} + H^+ + e^- \rightarrow OH_{ad}$ at $U = 1.0$ V, where at each point the charge is indicated.

the potential changes. This leads to a potential-dependent PES, as shown in Figure 9. As pointed out above, pathway 10 is also

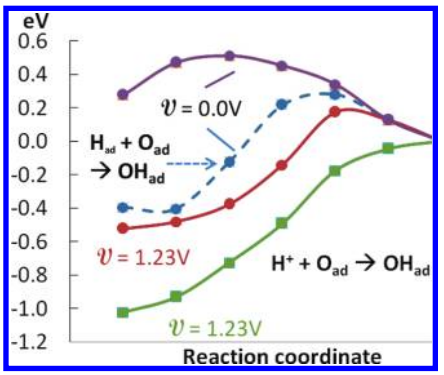

Figure 9. Optimal energy surface for $H^+ + O_{ad} \rightarrow OH_{ad}$ for various electrode potentials. Each line in this plot represents the "green" line selected from Figures 6–8. For simplicity, we show only the three typical cases with an imaginary dotted line based on the assumption that the reaction is from H^+. Solid lines show the PES for $O_{ad} + H^+$, whereas the dashed line is for $H_{ad} + O_{ad}$. For $U = 0.8$ and 1.23 V, the reaction starts with H^+. For $U = 0.0$ V, the reaction starts with H_{ad} (the blue dash line) because it is below the reversible potential of $H^+ \leftrightarrow H_{ad}$ and hence H_{ad} is the preferred form. We also included the hypothetical PES for $O_{ad} + H^+$ for $U = 0.0$ V (the purple line).

plausible, especially at low electrode potentials. Hence we also calculated the barrier to form OH directly from H_{ad} and O_{ad} to be 0.82 eV without solvation. As discussed in our previous works,[11,32] the barrier in solvent increases dramatically to 1.23 eV. However, it is also possible for the two steps in reaction 10 to occur concertedly; that is, H_{ad} migrates to a H_2O in solution phase, whereas the same water transfers a hydrogen to the O_{ad} to form OH_{ad}. This gives a barrier of 0.68 eV independent of the electrode potential.

Combining all of these processes leads to the potential-dependent energy surface for $U = 0.0$, 0.8, and 1.23 V, as shown in Figure 9. This makes reaction 10 less likely and leads to an increased reaction enthalpy and barrier for reaction 9. At $U = 0.0$ V, the preferred pathway is to form OH_{ad} from O_{ad} and H_{ad} with a corresponding barrier of 0.68 eV. As U increases, the

dx.doi.org/10.1021/jp207526u | J. Phys. Chem. C 2012, 116, 6166–6173

barrier increases as well, making the H_{ad} and OH formation from H^+ progressively unfavorable. At U = 0.8 V (the normal operating conditions), the direct formation from H^+ is preferred with a barrier of 0.70 eV.

Figure 10 shows the optimal enthalpic barrier for the reaction starting from both H^+ and H_{ad} at different electrode potentials.

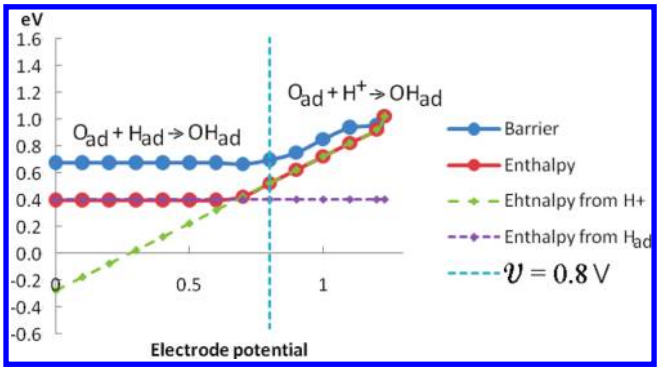

Figure 10. Potential-dependent barrier for $H^+ + O_{ad} \rightarrow OH_{ad}$. Each point in the barrier line represents the transition state (TS) point (the highest energy point in Figures 8 and 9), whereas each point in the enthalpy curve represents the difference between the starting and ending points. The barrier is the preferred one of reaction paths 8 and 9.

We see that at lower potential the stability of H_{ad} leads to a reaction with a constant barrier of 0.68 eV. At U > 0.7 V, H_{ad} becomes less favorable due to reaction A, and the barrier increases as H^+ becomes more and more stable.

We can see that reaction 10 is preferred for U < 0.67 eV because of the stability of H_{ad} as compared with H_3O^+. Therefore, at U = 0.0 V, an adsorbed H_3O^+ would transfer the H^+ to become $H_{ad} + H_2O_{ad}$, which would then react with O_{ad} either directly or indirectly via H_2O. This process is favorable for U < 0.67 V. Therefore, at the potential range from 0.0 to 0.67 V the reaction proceeds as $O_{ad} + H_3O^+ \rightarrow O_{ad} + H_2O + H_{ad} \rightarrow OH_{ad} + H_2O_{ad}$, whereas at higher potential, U > 0.67 V, as $H_3O^+ + O_{ad} \rightarrow OH_{ad} + H_2O_{ad}$. According to our calculations,[32] the barrier for direct formation of OH_{ad} from O_{ad} and H_{ad} is high, 0.97 eV. Because the barrier for $H^+ + e^- \rightarrow H_{ad}$ is always smaller than that of $H^+ + O_{ad} \rightarrow OH_{ad}$, the H^+/H_{ad} concentrations might be considered as always being at equilibrium. The one-step reaction $H^+ + O_{ad} \rightarrow OH_{ad}$ is preferred because the corresponding barrier is always smaller than 0.97 eV. Therefore, the actual OH formation mechanism depends on the potential range

$$H^+ \rightarrow H_{ad} \rightarrow OH_{ad} \text{ (via } H_2O\text{) for } U \text{ from 0.0 to 0.67 V}$$

$$H^+ + O_{ad} \rightarrow OH_{ad} \text{ for } U > 0.67 \text{ V}$$

Water Formation Reaction $H_3O^+ + OH_{ad} \rightarrow 2H_2O_{ad}$ (Step D of the ORR). The reaction enthalpy of the water formation

$$H_3O^+(\text{solv}) + OH_{ad}(\text{solv}) \rightarrow 2H_2O_{ad}(\text{solv}) \quad (11)$$

from surface H_3O^+ and OH_{ad} is calculated to be $\Delta H = -1.15$ eV at U = 0.0 V. Figure 11 demonstrates the energy surface of the reaction starting from H_{ad} at U = 0.0, 0.8, and 1.23 V, whereas Figure 12 shows the calculated enthalpy and barriers for this process for U up to 1.23 V, the experimental potential for H_2 oxidation (the calculated value is 1.33 V). Because of the exothermic nature, the reaction has no barrier for U < 1.15 V

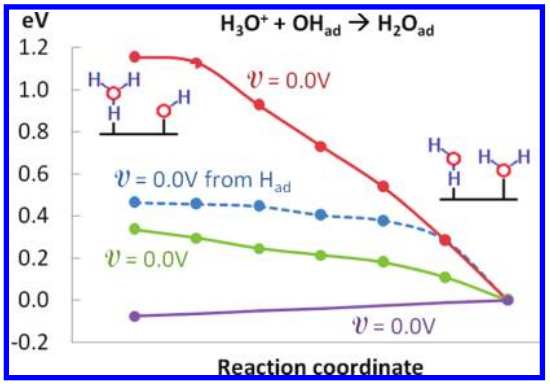

Figure 11. Potential-dependent PES for H_2O formation. Solid lines represent $H_3O^+ + OH \rightarrow 2H_2O$, whereas dotted lines represent $H_{ad} + OH \rightarrow H_2O$.

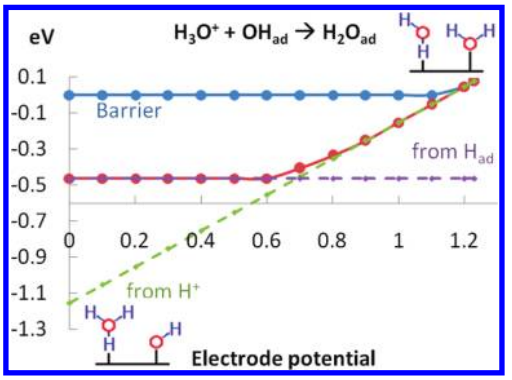

Figure 12. Potential-dependent barriers for H_2O formation.

and H_{ad} is the preferred form for U < 0.67 eV (Figure 11), lowering the reaction enthalpy over this range to −0.46 eV. As the electrode potential reaches the value over 0.67 eV, H_3O^+ reacts directly with OH_{ad} to form H_2O_{ad}.

Overall Oxygen Reduction (ORR) Reaction. Using the relationship among energy, charge, and the external potential (Computational Methods), we performed systematical calculations for reactions A−D for U from 0.0 to +1.2 V with an increment of 0.1 and calculated the energy surface at various electrode potentials. Figures 4, 9, and 11 show the PES at various electrode potential U, whereas Figure 13 summarizes the net barrier as a function of external potential. For reaction C, the barrier E_a = 0.68 eV and the enthalpy change ΔH = 0.40 eV are independent of the external potential up to U = 0.6 eV (Figure 10) because H_{ad} is either more stable or slightly less stable than H^+. Then, for U from 0.6 to 1.2 V, the ΔH increases linearly to 0.95 eV at 1.23 V, whereas the barrier increases monotonically to 0.96 eV at 1.23 V. This occurs because H^+ becomes increasingly more stable than H_{ad}, and the reaction becomes increasingly endothermic.

Figure 13 shows that OH formation dominates the ORR throughout the whole range of the electrode potential from 0.0 to 1.23 V. The barriers for reaction A and D can also be found in this Figure.

Therefore, the enthalpies for the four steps of the ORR are following

$$\Delta H_A = -0.44(-0.66) \text{ eV} + eU \quad (12)$$

$$\Delta H_B = -3.68 \text{ eV} \quad (13)$$

dx.doi.org/10.1021/jp207526u | J. Phys. Chem. C 2012, 116, 6166−6173

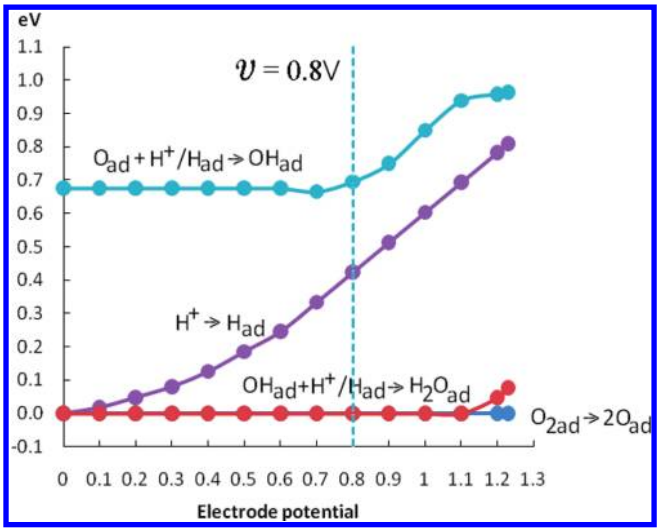

Figure 13. Barriers for reactions A–D, the four steps involved in the ORR. In general, all barriers become higher as electrode potential increases. Here OH formation is the RDS for ORR.

$$\Delta H_C = -0.28(-0.47)\ \text{eV} + eU \tag{14}$$

$$\Delta H_D = -1.15(-1.02)\ \text{eV} + eU \tag{15}$$

Here the numbers −0.44, −0.28, and −1.15 eV, are the energies for the system evolving from H^+ near the surface, whereas the numbers in parentheses are reaction enthalpy for the system evolving from solution phase H_2.

Comparison with Previous Approaches. By setting the reference potential to that of the NHE, Norskøv et al.[13] bypassed the direct handling of electron transfer, instead utilizing the known electrode potential dependence of reaction $H^+ + e^- \leftrightarrow 1/2H_2$ to estimate the energy of charged intermediates in terms of neutral energetics. This allows the enthalpy of each reaction step to be calculated from DFT calculations of non-electron-transfer reactions. By using $E_{F(U)} = E_{F(NHE)} + eU$, they were able to obtain electrode-potential-dependent reaction enthalpy and concluded that the overpotential arises from the OH formation step that becomes enthalpically unfavorable at high electrode potential. However, this method lacks the flexibility to handle arbitrary numbers of electrons and hence is not suitable for the study of TS or barriers of reactions, where the charge of the system is fractional and mostly undetermined.

An alternate approach was used by Anderson et al.,[12,14] who considered a finite system, where the energy of a charged system can be calculated exactly. They calculated the PES of the reaction with different charges and assumed that the crossing point of the two curves is both the electron-transfer step and the TS. Their small cluster (just Pt_2 in refs 12 and 14) leads to a finite gap (not a metal), so they approximate the Fermi level of the system as the average of ionization potential and electron affinity. The PES at various applied potentials can be deduced from the same calculation, leading to a potential-dependent barrier. However, the description of the catalytic surface as a small cluster (two atoms) and the approximation for the Fermi level makes the application of this method to the ORR system quite uncertain.

Neurock et al.[9,35,36] developed a double reference method where a compensating background charge is added to the semi-infinite slab system with a thick layer of water on top of the slab to allow a partial charge. The electrons involved are assumed to go to the Fermi level with the energy of the surface work function. A vacuum point far from the water coverage is used as the reference point for integrating the work function curve. For a charged system, such a reference cannot be compared directly, so the same integration is matched with that of the uncharged system based on the assumption that the work function in the water layer remains the same independent of the electrode potential.

The Neurock model has three major drawbacks. First, the solvation effects are modeled by a given number of water layers in the ice-like structure, which does not represent the real configuration of water around the reaction center, especially for the first two layers. Second, the coexistence of the vacuum region and the background charge leads to a net dipole perpendicular to the surface that makes the work function calculation unreliable and may also affect the geometry optimizations and barrier calculations. Third, there is little evidence of the validity of the work function integration across the vacuum–water interface.

Previously, we developed an implicit solvation model[11] based on the Poisson–Boltzmann continuum solvent method. We found that this method reproduces the solvent effect for solvation by explicit waters and can be expanded to cases where explicit solvation cannot be handled easily without molecular dynamics simulations. This implicit solvent method allows modeling of solvent effect for arbitrary surface species and spatial configurations and hence provides a consistent way of handling solvation across all reaction steps involved in ORR.

To solve the problem of having a net dipole perpendicular to the surface, Schultz developed the LMCC method[21,22] in which a carefully tailored background charge is added to balance the net charge, the dipole moment, and the dipole derivative. To avoid the difficulty of describing the work function without having a universal reference point and the problem of obtaining a well-defined integral across vacuum–water and water–metal interfaces, we add an empirical correction based on the energetics for $H^+ \leftrightarrow H_2$ corresponding to the NHE. This leads to a corrected DFT Fermi level that is consistent with the NHE comparison.

Combining these various approaches together, we developed a systematical approach capable of handling the reaction steps involving electron transfer while including the effect of solvation and the external electrochemical potential. This allows consistent calculation for all reaction steps in a surface reaction independent of whether electron transfer is involved.

Optimal Power. Figure 13 shows the barriers for the ORR steps A, C, and D compared with the potential-independent barrier for step B. For all cases, the RDS is step 14.

Because the total current is

$$I = A\cdot\exp(-E_{a,RDS}(U)/RT)$$

the total power is

$$P = I\cdot V = A\cdot V\cdot\exp(-E_{a,RDS}(U)/RT)$$

which is plotted as a function of U in Figure 14. Here we see that the optimal potential is predicted to be 0.68 V, which is close to the standard fuel cell operating voltage of ~0.8 V (which we assume is the experimental optimum). The difference of 0.12 V could arise from a number of simplifications in our analysis regarding the form of the pre-exponential parameters, approximations for solvation, ignoring of the double-layer effect, and inaccuracy of the DFT method. The good agreement between the experimental and computationally

dx.doi.org/10.1021/jp207526u | J. Phys. Chem. C 2012, 116, 6166–6173

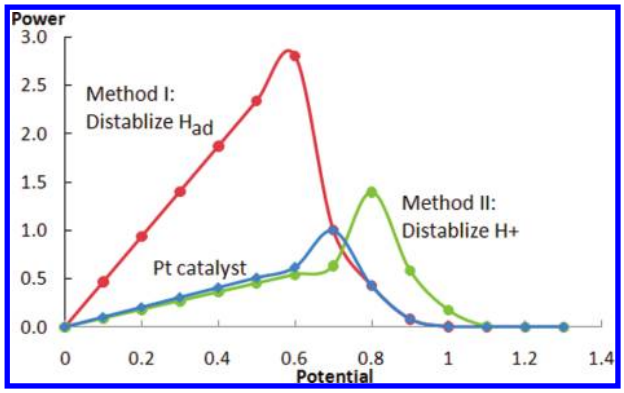

Figure 14. Predicted power output as a function of electrode potential. Here we also consider the impact of small changes in the energetics. The red line shows the effect of destabilizing H_{ad} by 0.05 eV, which leads to an increase in efficiency by a factor of 2.8. The blue line shows the effect of destabilizing H_3O^+ by changing the dielectric constant from 80 to 40.

predicted values for the optimal potential validates our approach and approximations applied in this work.

On the basis of the expression relating the overall power or efficiency to the fundamental barriers of the ORR mechanism, we now examine how changes in the alloys might modify the total power and optimum operating potential. For example, if we could modify the catalyst to decrease the barrier for the OH_{ad} formation from H_{ad} by 0.05 eV, then according to Figure 14 the power would improve by a factor of 2.81 and the optimal operating potential would drop by 0.08 V to U_{opt} = 0.60 V. Such a change in the barrier could also be achieved by making H_{ad} less stable, by 0.10 eV, using, for instance, metal alloy. (Ni binds H by 0.34 eV less strongly than Pt, and it is well known that Pt_3Ni has improved ORR rates.[44])

Alternatively, H^+ might be destabilized relative to H_{ad} by modifying the electrolyte, solvent (decreasing the dielectric constant), or pH. For example, changing the effective dielectric constant from 80 (H_2O) to 40 (CH_3CN) would destabilize H^+ by 0.12 eV, which leads to an increase in the optimal voltage by 0.12 V to U = 0.80 V and to an improvement in optimal power by a factor of 1.40.

CONCLUDING REMARKS

In this Article, we propose a systematic DFT approach to handle the barriers of electron transfer reactions (e.g., $H^+ + e^- + O_{ad} \rightarrow OH_{ad}$). This methodology was applied to examine the potential dependence of the various steps involved in the ORR. We used these results to estimate the optimum operating electrochemical potential for a Pt-catalyzed PEMFC. On the basis of our mechanism and calculated barriers, we estimate the optimum operating voltage for the ORR on Pt to be 0.68 V/NHE, which is close to the standard operating voltage of ~0.8 V/NHE. The good agreement of the computationally predicted values of the optimal potential with experimental validates our approach and approximations. A full analysis of the fuel cell efficiency involves a number of factors including the electric double-layer effect and surface concentrations within the solvent monolayer next to the catalyst and of the chemisorbed species on the catalyst. An additional factor, which affects the fuel cell efficiency and which was ignored in our work, is the concentration of H_3O^+ in the membrane that depends on the operating conditions such as water content, nature of the membrane, temperature, pressure, and so on. However, starting with the results reported herein may provide a useful framework for examining these additional issues.

For Pt, our results suggest that step C (OH-formation) is the RDS. Therefore, to improve the ORR rates, one should focus on improving step C. Finding a catalyst with a weaker O binding energy could make the OH formation easier. It is also desirable to make the O_2 dissociation faster. For surfaces that are not composed of Pt or Pd, it might be good to decrease the OH binding energy to make the H_2O formation exothermic at potential above 0.8 V.

We proposed recently[32] an alternative for OH_{ad} production, namely, hydrolysis of O_{ad}

$$O_{ad} + H_2O_{ad} \rightarrow 2OH_{ad}$$

This reaction has a barrier of 0.50 eV in water solvent and should be favorable for low proton concentrations. Similarly, for the low proton concentrations the reverse reactions

$$H_2O \rightarrow OH + H^+ \text{ and } OH \rightarrow O + H$$

might be an important issue limiting the power.

AUTHOR INFORMATION

Corresponding Author

*E-mail: wag@wag.caltech.edu.

Notes

The authors declare no competing financial interest.

ACKNOWLEDGMENTS

This work was partially supported by the National Science Foundation under grant CBET-1067848 (Program Manager: Dr. George Antos) and partially by Ford Motor Company (Dr. Pezhman Shirvanian). The facilities of the MSC used in this study were established with grants from DURIP-ONR, DURIP-ARO, and NSF-CSEM.

REFERENCES

(1) Kordesch, K.; Simader, G. *Fuel Cells and Their Applications*; VCH: New York, 1996.
(2) Appleby, A.; Foulkes, F. *Fuel Cell Handbook*; Van Nostrand Reinhold: New York, 1989.
(3) Brandon, N. P.; Skinner, S.; Steele, B. C. H. *Annu. Rev. Mater. Res.* **2003**, *33*, 183–213.
(4) Mehta, V.; Cooper, J. S. *J. Power Sources* **2003**, *114*, 32–53.
(5) Wang, X. G.; Fisher, G. B. *Phys. Rev. Lett.* **2007**, *99*, 66101.
(6) Zhang, T.; Anderson, A. B. *J. Phys. Chem. C* **2007**, *111*, 8644–8648.
(7) Rai, V.; Aryanpour, M.; Pitsch, H. *J. Phys. Chem. C* **2008**, *112*, 9760–9768.
(8) Greeley, J.; Norskov, J. K. *J. Phys. Chem. C* **2009**, *113*, 4932–4939.
(9) Janik, M. J.; Taylor, C. D.; Neurock, M. *J. Electrochem. Soc.* **2009**, *156*, B126–B135.
(10) Ford, D. C.; Nilekar, A. U.; Xu, Y.; Mavrikakis, M. *Surf. Sci.* **2010**, *604*, 1565–1575.
(11) Sha, Y.; Yu, T. H.; Liu, Y.; Merinov, B. V.; Goddard, W. A. *J. Phys. Chem. Lett.* **2010**, *1*, 856–861.
(12) Cai, Y.; Anderson, A. *J. Phys. Chem. B* **2005**, *109*, 7557–7563.
(13) Norskov, J. K.; Rossmeisl, J.; Logadottir, A.; Lindqvist, L.; Kitchin, J. R.; Bligaard, T.; Jonsson, H. *J. Phys. Chem. B* **2004**, *108*, 17886–17892.
(14) Cai, Y.; Anderson, A. B. *J. Phys. Chem. B* **2004**, *108*, 9829–9833.
(15) Schultz, P. *SeqQuest Code Project*; Sandia National Laboratories: Albuquerque, NM. http://www.cs.sandia.gov/~paschul/Quest/.
(16) Melius, C. F.; Goddard, W. A. *Phys. Rev. A* **1974**, *10*, 1528–1540.

(17) Melius, C. F.; Olafson, B. D.; Goddard, W. A. *Chem. Phys. Lett.* **1974**, *28*, 457−462.
(18) Redondo, A.; Goddard, W. A.; Mcgill, T. C. *Phys. Rev. B* **1977**, *15*, 5038−5048.
(19) Hamann, D. R. *Phys. Rev. B* **1989**, *40*, 2980−2987.
(20) Perdew, J.; Burke, K.; Ernzerhof, M. *Phys. Rev. Lett.* **1996**, *77*, 3865−3868.
(21) Schultz, P. A. *Phys. Rev. B* **1999**, *60*, 1551−1554.
(22) Schultz, P. A. *Phys. Rev. Lett.* **2000**, *84*, 1942−1945.
(23) Tomasi, J.; Persico, M. *Chem. Rev.* **1994**, *94*, 2027−2094.
(24) Cramer, C.; Truhlar, D. *Chem. Rev.* **1999**, *99*, 2161−2200.
(25) Baker, N. A.; Sept, D.; Joseph, S.; Holst, M. J.; McCammon, J. A. *Proc. Natl. Acad. Sci. U.S.A.* **2001**, *98*, 10037−10041.
(26) Holst, M.; Saied, F. *J. Comb. Chem.* **1995**, *16*, 337−364.
(27) Holst, M.; Saied, F. *J. Comput. Chem.* **1993**, *14*, 105−113.
(28) Goddard, W. A.; Jaramillo-Botero, A.; Liu, Y.; Duin, A. v.; Buehler, M.; Meulbroek, P.; Dodson, J. *The Computational Materials Design Facility (CMDF) Project*. http://www.wag.caltech.edu/multiscale/multsicale_computations.htm.
(29) Rogstad, K. N.; Jang, Y. H.; Sowers, L. C.; Goddard, W. A. *Chem. Res. Toxicol.* **2003**, *16*, 1455−1462.
(30) Jones, C. J.; Taube, D.; Ziatdinov, V. R.; Periana, R. A.; Nielsen, R. J.; Oxgaard, J.; Goddard, W. A. *Angew. Chem., Int. Ed.* **2004**, *43*, 4626−4629.
(31) Nielsen, R. J.; Goddard, W. A. *J. Am. Chem. Soc.* **2006**, *128*, 9651−9660.
(32) Sha, Y.; Yu, T. H.; Merinov, B. V.; Shirvanian, P.; Goddard, W. A. *J. Phys. Chem. Lett.* **2011**, *2*, 572−576.
(33) Mills, G.; Jonsson, H.; Schenter, G. K. *Surf. Sci.* **1995**, *324*, 305−337.
(34) Mills, G.; Jonsson, H. *Phys. Rev. Lett.* **1994**, *72*, 1124−1127.
(35) Filhol, J. S.; Neurock, M. *Angew. Chem., Int. Ed.* **2006**, *45*, 402−406.
(36) Taylor, C. D.; Wasileski, S. A.; Filhol, J. S.; Neurock, M. *Phys. Rev. B* **2006**, *73*, 165402.
(37) Mejias, J. A.; Lago, S. *J. Chem. Phys.* **2000**, *113*, 7306−7316.
(38) Kötz, E.; Neff, H.; Müller, K. *J. Electroanal. Chem. Interfacial Electrochem.* **1986**, *215*, 331−344.
(39) Thalinger, M.; Volmer, M. *Z. Phys. Chem., Abt. A* **1930**, *150*, 401−417.
(40) Marcus, R. A.; Sutin, N. *Biochim. Biophys. Acta* **1985**, *811*, 265−322.
(41) Peremans, A.; Tadjeddine, A. *J. Chem. Phys.* **1995**, *103*, 7197−7203.
(42) Olsen, R.; Kroes, G.; Baerends, E. *J. Chem. Phys.* **1999**, *111*, 11155−11163.
(43) Balakrishnan, A.; Smith, V.; Stoicheff, B. P. *Phys. Rev. Lett.* **1992**, *68*, 2149−2152.
(44) Stamenkovic, V. R.; Fowler, B.; Mun, B. S.; Wang, G. F.; Ross, P. N.; Lucas, C. A.; Markovic, N. M. *Science* **2007**, *315*, 493−497.